Passive wavefield imaging using the energy norm

Daniel Rocha and Paul Sava, Center for Wave Phenomena, Colorado School of Mines,
Jeffrey Shragge, Centre for Energy Geoscience, The University of Western Australia

SUMMARY

Wavefield imaging offers a robust approach for source evaluation in microseismic monitoring. The coexistence of P- and S- wavemodes at the source location after time-reversal leads to an imaging condition from which the source position and radiation pattern can be identified. We propose a new imaging condition that is based on energy conservation and is directly related to the source mechanism. Unlike the correlation between decomposed P- and S- wavefields typically used in passive elastic imaging, our imaging condition compares wavemodes present in the displacement field without costly wave-mode decomposition, and produces a strong and focused correlation at the source location. Numerical experiments demonstrate the advantages of the proposed imaging condition (compared to PS correlation), its sensitivity with respect to velocity inaccuracy and sparse acquisition, and its quality and efficacy in estimating the source location.

INTRODUCTION

Passive seismic monitoring uses signals caused by natural or induced seismicity to infer subsurface properties. The main difference from conventional exploration seismology is the absence of a controlled source. Although the seismic source location for passive seismic is not known, one can apply methods similar to those in active seismic acquisition to achieve an image and an Earth model (Duncan and Eisner, 2010; Maxwell et al., 2010; Xuan and Sava, 2010; Behura et al., 2013; Blias and Grechka, 2013; Witten and Shragge, 2015; Bazargani and Snieder, 2016). Microseismic monitoring is frequently used for description of unconventional reservoirs (Warpinski et al., 2012), and its most common application is for hydraulic fracturing. Fluid injection induces microseismic events, which can be observed by monitoring either from the surface or from boreholes. Using the recorded data, one can estimate the microseismic source location, and locate hydraulic fracturing in the subsurface (Maxwell, 2010; Michel and Tsvankin, 2013). Joint estimation of source location and mechanism potentially provides information about faults and fractures orientation (Zhebel and Eisner, 2012; Jeremic et al., 2014).

Wavefield imaging is usually implemented in two steps: (1) backpropagation of the recorded wavefield into the earth; and (2) application of an imaging condition to extract the source location and/or origin time (McMechan, 1982; Gajewski and Tessmer, 2005; Xuan and Sava, 2010; Nakata and Beroza, 2016). For multicomponent data, one typically employs imaging procedures that exploit the different wave modes present in elastic data. The spatial and temporal coexistence of P- and S- wavefields at the source allows for a PS imaging condition implemented in three steps: (1) backpropagation of the multicomponent wavefield; (2) wave-mode decomposition of the wavefield; and (3) the zero-lag crosscorrelation of the decomposed P- and S- wavefields (Artman et al., 2010; Witten and Artman, 2010; Douma and Snieder, 2015).

We propose an imaging condition for passive seismic data similar to the PS imaging condition, but without step (2) wave-mode decomposition. Our imaging condition attenuates the correlation between identical waves modes in the displacement field and highlights the correlation of different modes at the source. Based on energy conservation of elastic wavefields, we define an imaging condition as the difference between the kinetic and potential terms of a wavefield, which are computed using just the displacement field. This imaging condition is successful in elastic imaging with attenuated artifacts for active experiments, as shown in previous work (Rocha et al., 2016b,c). Here, we explain how a similar imaging condition is applicable to passive imaging, and we demonstrate its effectiveness in locating seismic sources using synthetic experiments in realistic settings.

THEORY

The anisotropic elastic wave equation is

$$\rho\ddot{\mathbf{U}} = \nabla\cdot\left[\underline{\mathbf{c}}\nabla\mathbf{U}\right] \ , \tag{1}$$

where $\mathbf{U}(\mathbf{x},t)$ is the displacement field as a function of space ($\mathbf{x}$) and time (t), $\rho(\mathbf{x})$ is the density, and $\underline{\mathbf{c}}(\mathbf{x})$ is the 4th-order stiffness tensor. The superscript dot indicates time differentiation. For an isotropic and slowly varying medium, equation 1 reduces to

$$\ddot{\mathbf{U}} = V_P^2\nabla\left(\nabla\cdot\mathbf{U}\right) - V_S^2\nabla\times\left(\nabla\times\mathbf{U}\right) \ , \tag{2}$$

where V_P and V_S are the P- and S- wave velocities, respectively. Using recorded multicomponent data, the displacement field $\mathbf{U}$ can be extrapolated in the subsurface using either equation 1 or 2 depending on the assumptions about the medium anisotropy. Our imaging condition works equally well for both types of wavefields.

Different imaging conditions using the displacement field directly have been proposed to estimate the source location. Steiner et al. (2008) propose to use the absolute value of the particle velocity. One can also implement wave-mode decomposition, i.e. separate the displacement field into P- and S- wavefields. For isotropic media, wave-mode decomposition is cheap and typically implemented by Helmholtz decomposition (Dellinger and Etgen, 1990; Yan and Sava, 2009):

$$P = \nabla\cdot\mathbf{U} \ , \tag{3}$$

$$\mathbf{S} = \nabla\times\mathbf{U} \ , \tag{4}$$

where $P(\mathbf{x},t)$ is a scalar wavefield containing the compressional wave mode, and $\mathbf{S}(\mathbf{x},t)$ is a vector wavefield containing the transverse wave mode. For anisotropic media, wave-mode decomposition is implemented by solving the Christoffel equation (Dellinger and Etgen, 1990); using techniques with significant additional cost (Yan and Sava, 2009, 2011; Cheng and Fomel, 2013).

Separated wave modes can be imaged using

$$I_{PP}(\mathbf{x}) = \sum_t P(\mathbf{x},t)\, P(\mathbf{x},t) \ , \tag{5}$$

$$I_{SS}(\mathbf{x}) = \sum_t \mathbf{S}(\mathbf{x},t) \cdot \mathbf{S}(\mathbf{x},t) \ . \tag{6}$$

These imaging conditions consist of an autocorrelation of a given wave mode, which produces low-wavenumber content along the path where the waves propagate. Alternatively, one can use different wave modes to form an image free of low-wavenumber artifacts. For a non-scattering medium, P- and S- waves propagate at different speeds and coexist in space and time only at the source (Yan and Sava, 2008; Artman et al., 2010):

$$\mathbf{I}_{PS}(\mathbf{x}) = \sum_t P(\mathbf{x},t)\, \mathbf{S}(\mathbf{x},t) \ . \tag{7}$$

$\mathbf{I}_{PS}(\mathbf{x})$ is a multicomponent image, whose components represent the correlation between $P(\mathbf{x},t)$ and the corresponding component from $\mathbf{S}(\mathbf{x},t)$. In 3-D, three images can be computed instead of a single one that concisely shows the source location.

In contrast to PS imaging, the energy norm (Rocha et al., 2016a,c) allows one to define an imaging condition for elastic reverse time migration (ERTM) that concisely exhibits the reflectors in subsurface. For passive imaging, in which only one wavefield is extrapolated, we can define an imaging condition as

$$I_E(\mathbf{x}) = \sum_t \left[\rho \dot{\mathbf{U}} \cdot \dot{\mathbf{U}} - \left(\underline{\mathbf{c}} \nabla \mathbf{U} \right) : \nabla \mathbf{U} \right] . \tag{8}$$

Although the imaging condition in equation 8 involves autocorrelation of the displacement field $\mathbf{U}$, the interaction between the same wave modes is attenuated as shown by Rocha et al. (2016b,c). The first and second terms in equation 8 represent the kinetic and potential wavefield energies, respectively. Equation 8 is related to the Lagrangian operator, which is expressed as the difference between kinetic and potential energy terms:

$$\mathcal{L}(\mathbf{U},\mathbf{x},t) = \frac{1}{2}\rho \dot{\mathbf{U}} \cdot \dot{\mathbf{U}} - \frac{1}{2} \left(\underline{\mathbf{c}} \nabla \mathbf{U} \right) : \nabla \mathbf{U} \ . \tag{9}$$

In the presence of sources, the Lagrangian for small displacement fields is associated with the action from these sources (Ben-Menahem and Singh, 1981):

$$\int_0^T \mathcal{L}(\delta\mathbf{U},\mathbf{x},t)\, dt = -\int_0^T \nabla \cdot (\underline{\mathbf{t}} \cdot \delta\mathbf{U})\, dt - \int_0^T \rho \mathbf{F} \cdot \delta\mathbf{U}\ dt \ , \tag{10}$$

where $\underline{\mathbf{t}}(\mathbf{x},t)$ and $\mathbf{F}(\mathbf{x},t)$ are external stress or body forces, respectively. Equation 10 implies that, at the source, the imaging condition in equation 8 is directly related to the source mechanism.

Moreover, the energy imaging condition for passive imaging correlates P- and S- modes using the displacement field directly, without wave-mode decomposition. For isotropic media, the costs of the PS imaging condition (equation 7) and the energy imaging condition (equation 8) are comparable, since in both cases one needs to compute wavefield derivatives; for anisotropic media, computing equation 8 is quite cheaper than decomposing modes during extrapolation.

EXAMPLES

An imaging condition for passive seismic should deliver a strong and focused correlation at the source location if true model parameters are used. Figure 1a shows an ideal 2-D passive experiment where multicomponent receivers surround the source from all possible angles. The source mechanism consists of a stress field generated by a fault displacement oriented at 45° with respect to the horizontal. Note that the energy imaging condition (Figure 1e) results in a stronger and more focused correlation at the source location compared to the PS imaging condition (Figure 1c).

Figure 1b shows a similar experiment geometry but containing a sparse array of receivers only at the surface. The PS (Figure 1d) and energy images (Figure 1f) have similar resolution and quality considering the same acquisition limitations. In addition, Figures 1d and 1f illustrate that one should consider smearing and truncation artifacts when estimating a source location using wavefield imaging methods for passive seismic, since acquired data capture an incomplete wavefield, which prevents the extrapolated waves from collapsing into a focal point.

Figure 2 shows the effect of the source mechanism on PS and energy images, for a geometry similar to Figure 1b but with receivers at every grid point of the surface. For sources describing fault or fracture planes at steep angles (Figures 2c-2f), both imaging conditions show smearing along their source orientation. For a horizontal source (Figures 2a-2b), the energy image exhibits better focusing compared to the PS image. The analysis of radiation patterns for different source orientations is important because it can help us infer the fault slip or fracture direction.

We also illustrate our method with the Marmousi II model (Martin et al., 2002) in order to simulate more realistic passive acquisition in an area subject to hydraulic fracturing (Figure 3). The experiment consists of a microseismic source representing a fracture oriented at 30° (Figure 3a). Data are recorded with an array of multicomponent receivers with 80 m spacing in a borehole, and another array of receivers with 40 m receiver

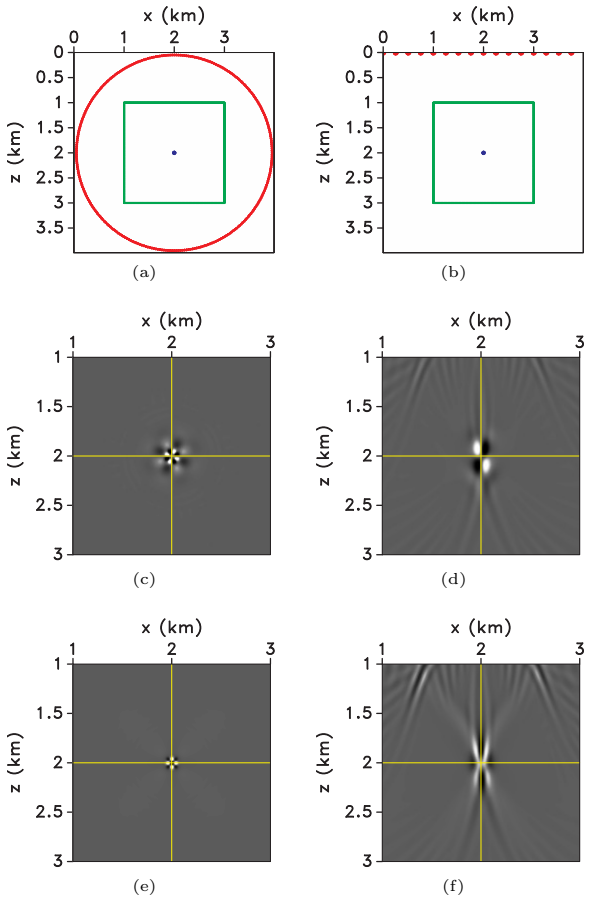

Figure 1: (a) Circular acquisition with equal coverage from all angles and (b) with sparse coverage at the surface only. Multicomponent receivers in red, stress source oriented by 45° in the center, and zoom area represented by the box. PS images (c)-(d), and energy images (e)-(f) for the circular and surface acquisition, respectively. Using the circular acquisition, the energy image in (e) has a strong and focused peak at the source location compared to the PS image in (c). Using the sparse surface acquisition, the PS (d) and energy (f) images are comparable in quality and show truncation artifacts compared to the images in (c) and (e).

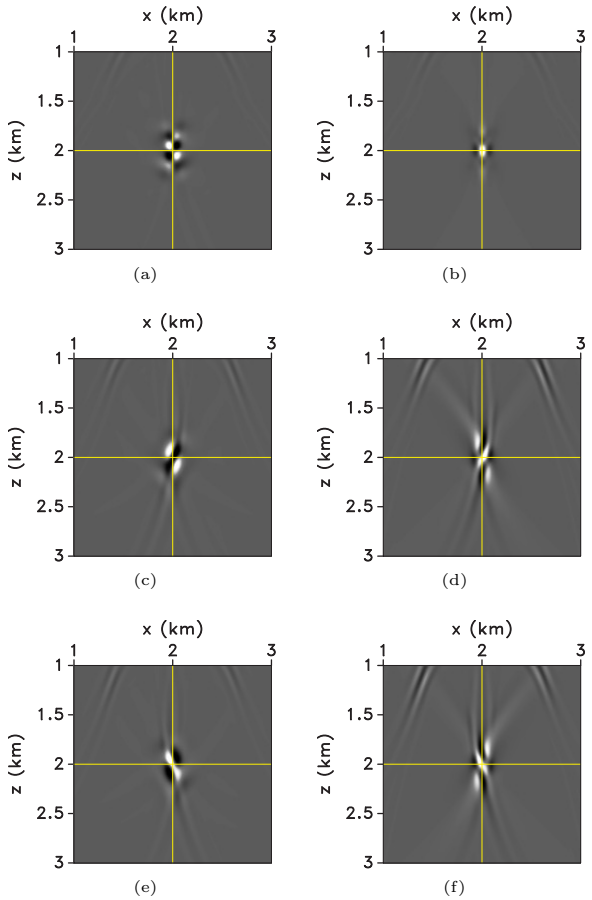

Figure 2: Radiation patterns for the acquisition with complete surface coverage. PS images for a stress source oriented at (a) 0°, (c) 30°, and (e) 60°. Energy images for a stress source oriented at (b) 0°, (d) 30°, and (f) 60°. Both PS and energy imaging condition have analogous radiation patterns, with exception to 0°, where the energy image exhibits better focusing.

spacing on the surface. The combination of surface and borehole arrays improves passive seismic results due to the larger effective acquisition aperture (Thornton and Duncan, 2012). The Marmousi II model contains P and S velocities (Figure 3b) that are not proportional to each other, i.e., a spatially variable velocity ratio (V_P/V_S) (Figure 3c). We smooth the velocities to obtain only P and S direct arrivals in the synthetic data and we further smooth the velocities and scale by 2% to simulate inaccurate migration velocity.

Figures 3d-3f show the application of the PS and energy imaging conditions when using the correct velocity. In Figure 3d, the energy correlation is strong at the source location compared to the surrounding artifacts, which is not the case for the corresponding PS image. Comparing the zoomed images (Figures 3e and 3f), note that the energy image is more focused at the source location than the PS image. In Figure 3f, the smearing in the source correlation compared to the radiation patterns in Figure 2d and 2f potentially infers that the source mechanism is due to an oblique fracture, which matches the simulated stress source oriented at 30°. Using the incorrect velocity (Figures 3g-3i), the artifacts increase and both images are more unfocused (Figures 3h and 3i), although the energy image retains partially its shape from the accurate velocity case. The Marmousi II experiment demonstrates that the energy imaging condition involves an indirect correlation of P and S waves that produces a stronger correlation at the source location compared to the direct PS correlation.

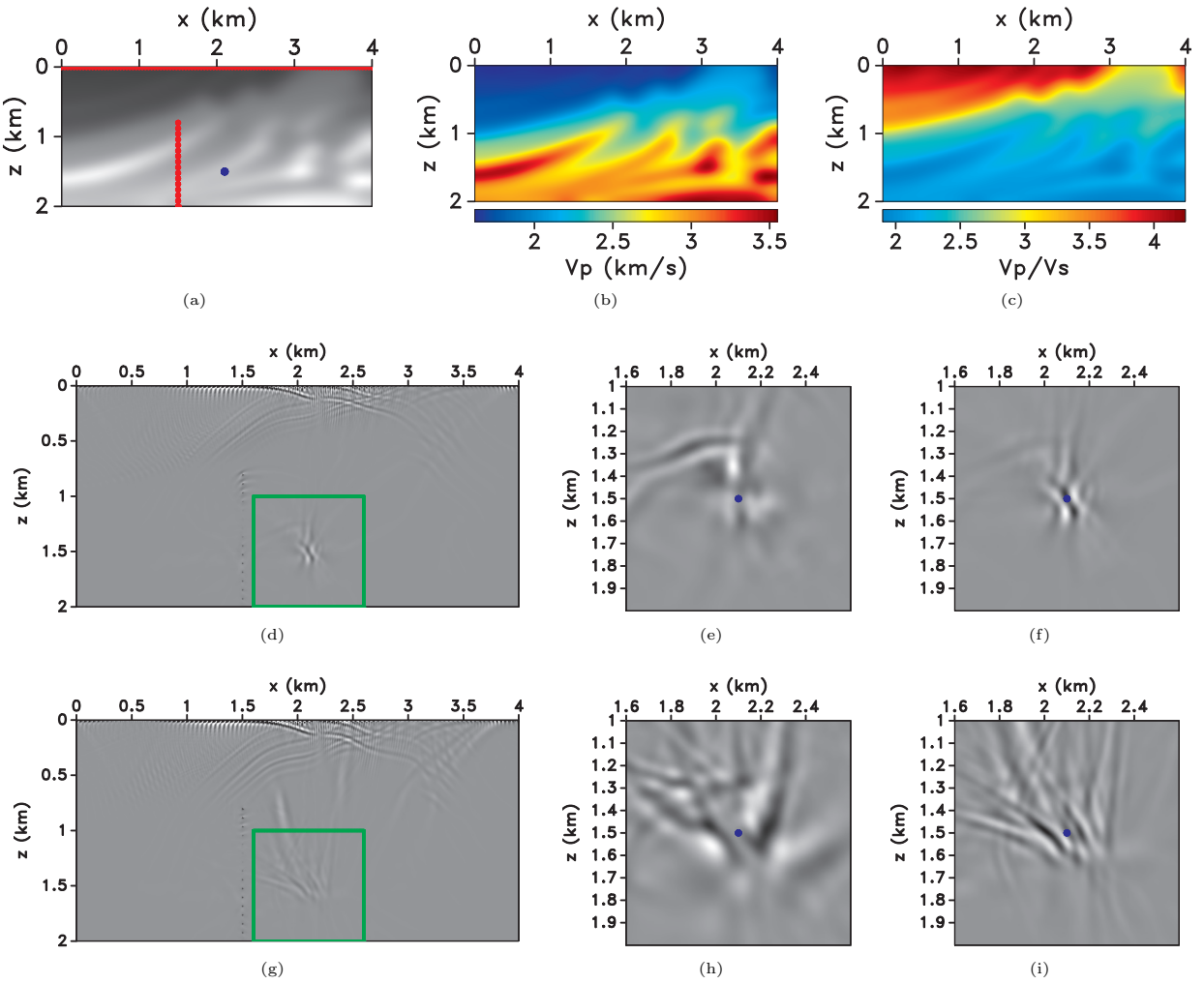

Figure 3: Acquisition geometry for the Marmousi-II experiment (a) with receivers in red and the source in blue color. (b) True P- wave velocity, and (c) true PS velocity ratio. (d) Complete energy image, and zoomed (e) PS and (f) energy images for correct velocity. (g) Complete energy image, and zoomed (h) PS and (i) energy images for incorrect velocity.

CONCLUSIONS

For passive wavefield imaging with multicomponent data, the energy imaging condition offers an elegant solution to locate seismic sources for an arbitrary Earth model. In contrast, the PS imaging condition requires a costly decomposition of the wavefields in Earth models that incorporate anisotropy. Based on the energy conservation for extrapolated wavefields, our imaging condition represents the temporal integral of the Lagrangian operator (which is the difference between kinetic and potential terms from the wavefield) and produces an image that is directly related to the source mechanism. We demonstrate for simple models that the energy and PS imaging conditions are comparable in terms of image quality and characterization of radiation patterns. For more realistic settings, we show that the energy imaging condition handles imaging artifacts and source focusing better than its conventional PS counterpart. Future work involves exploring the cost and further benefits of the energy imaging condition for anisotropic media, and developing a velocity inversion procedure using the unfocused energy on extended image gathers.

ACKNOWLEDGEMENTS

We thank the sponsors of the Center for Wave Phenomena, whose support made this research possible. The reproducible numeric examples in this paper use the Madagascar open-source software package (Fomel et al., 2013) freely available from http://www.ahay.org.

REFERENCES

Artman, B., I. Podladtchikov, and B. Witten, 2010, Source location using time-reverse imaging: Geophysical Prospecting, **58**, 861–873.

Bazargani, F., and R. Snieder, 2016, Optimal source imaging in elastic media: Geophysical Journal International, **204**, 1134–1147.

Behura, J., F. Forghani, and F. Bazargani, 2013, Improving microseismic imaging: role of acquisition, velocity model, and imaging condition: Presented at the SEG Houston 2013 Annual Meeting.

Ben-Menahem, A., and S. J. Singh, 1981, Seismic waves and sources, 1 ed.: Springer-Verlag.

Blias, E., and V. Grechka, 2013, Analytic solutions to the joint estimation of microseismic event locations and effective velocity model: Geophysics, **78**, KS51–KS61.

Cheng, J., and S. Fomel, 2013, Fast algorithms for elastic-wave-mode separation and vector decomposition using low-rank approximation for anisotropic media: Presented at the SEG Houston 2013 Annual Meeting.

Dellinger, J., and J. Etgen, 1990, Wave-field separation in two-dimensional anisotropic media: Geophysics, **55**, 914–919.

Douma, J., and R. Snieder, 2015, Focusing of elastic waves for microseismic imaging: Geophysical Journal International, **200**, 390–401.

Duncan, P., and L. Eisner, 2010, Reservoir characterization using surface microseismic monitoring: Geophysics, **75**, A139–A146.

Fomel, S., P. Sava, I. Vlad, Y. Liu, and V. Bashkardin, 2013, Madagascar: open-source software project for multidimensional data analysis and reproducible computational experiments: Journal of Open Research Software, **1**.

Gajewski, D., and E. Tessmer, 2005, Reverse modelling for seismic event characterization: Geophysical Journal International, **163**, 276–284.

Jeremic, A., J. Kurpan, M. Thornton, and M. Mueller, 2014, Extending passive seismic imaging to account for source mechanism effects: Presented at the SEG Denver 2014 Annual Meeting.

Martin, G., K. Marfurt, and S. Larsen, 2002, Marmousi-2, an updated model for the investigation of avo in structurally complex areas: Presented at the 2002 SEG Annual Meeting.

Maxwell, S., 2010, Microseismic: Growth born from success: The Leading Edge, **29**, 338–343.

Maxwell, S., J. Rutledge, R. Jones, and M. Fehler, 2010, Petroleum reservoir characterization using downhole microseismic monitoring: Geophysics, **75**, A129–A137.

McMechan, G. A., 1982, Determination of source parameters by wavefield extrapolation: Geophysical Journal International, **71**, 613–628.

Michel, O. J., and I. Tsvankin, 2013, Gradient computation for full-waveform inversion of microseismic data in vti media: Presented at the SEG Houston 2013 Annual Meeting.

Nakata, N., and G. C. Beroza, 2016, Reverse time migration for microseismic sources using the geometric mean as an imaging condition: Geophysics, **81**, KS51–KS60.

Rocha, D., N. Tanushev, and P. Sava, 2016a, Acoustic wavefield imaging using the energy norm: Geophysics (accepted for publication).

———, 2016b, Anisotropic elastic wavefield imaging using the energy norm: Presented at the 78th EAGE Conference and Exhibition.

———, 2016c, Isotropic elastic wavefield imaging using the energy norm: Geophysics (accepted for publication).

Steiner, B., E. H. Saenger, and S. M. Schmalholz, 2008, Time reverse modeling of low-frequency microtremors: Application to hydrocarbon reservoir localization: Geophysical Research Letters, **35**, L03307.

Thornton, M., and P. Duncan, 2012, Microseismic imaging with combined surface and downhole arrays: Presented at the SEG Las Vegas 2012 Annual Meeting.

Warpinski, N., J. Du, and U. Zimmer, 2012, Measurements of hydraulic-fracture-induced seismicity in gas shales: Presented at the SPE Hydraulic Fracturing Technology Conference.

Witten, B., and B. Artman, 2010, Signal-to-noise estimates of time-reverse images: Presented at the SEG Denver 2010 Annual Meeting.

Witten, B., and J. Shragge, 2015, Extended wave-equation imaging conditions for passive seismic data: Geophysics, **80**, WC61WC72.

Xuan, R., and P. Sava, 2010, Probabilistic microearthquake location for reservoir monitoring: Geophysics, **75**, MA9–MA26.

Yan, J., and P. Sava, 2008, Isotropic angle-domain elastic reverse-time migration: Geophysics, **73**, S229–S239.

———, 2009, Elastic wave-mode separation for VTI media: Geophysics, **74**, WB19–WB32.

———, 2011, Elastic wave-mode separation for tilted transverse isotropy media: Geophysical Prospecting, **60**, 29–48.

Zhebel, O., and L. Eisner, 2012, Simultaneous microseismic event localization and source mechanism determination: Presented at the SEG Las Vegas 2012 Annual Meeting.